

A Bayesian Approach to Nonlinear Inversion: Abel Inversion from X-Ray Attenuation Data

KENNETH M. HANSON Los Alamos National Laboratory, Los Alamos, New Mexico

With a change of variables the Abel transform gives the projection of a 2-D distribution with circular symmetry. Thus the Abel inversion formula allows one to determine the radial dependence of such a distribution from its projection. However, this inversion formula is very sensitive to noise in the projection data. When the projection data are derived from radiographic measurements, further difficulties arise from the necessity to invert the exponential dependence of the measured x-radiation intensity upon material thickness. These difficulties are shown to be overcome by applying a maximum a *posteriori* (MAP) method, which was developed to accommodate nonlinear measurements, to this tomographic reconstruction problem. The MAP method yields a smooth solution in regions where the signal-to-noise ratio is low while maintaining good spatial resolution in regions where it is high.

1 Introduction

In 1826 Abel [1] provided a method for recovering the density distribution of a two-dimensional, circularly symmetric object from its projection. It is possible to extend this 2-D analysis to reconstruct the cross section of a three-dimensional, axially symmetric object from a single radiograph, as depicted in Fig. 1. In industrial radiography, where many objects have nearly circular symmetry, such an approach offers significant benefits as an image analysis tool [2]. These benefits include improved delineation of material boundaries, enhanced display of deviations from axial symmetry (e. g., possibly caused by defects), and estimation of the radial dependence of the attenuation coefficients of the materials. It is often possible to observe in the reconstruction subtle features of the object that are unobservable in the original radiograph. The improvements brought about by the tomographic method are due to the effective removal of overlying material

This work was supported by the United States Department of Energy under contract number W-7405-ENG-36.

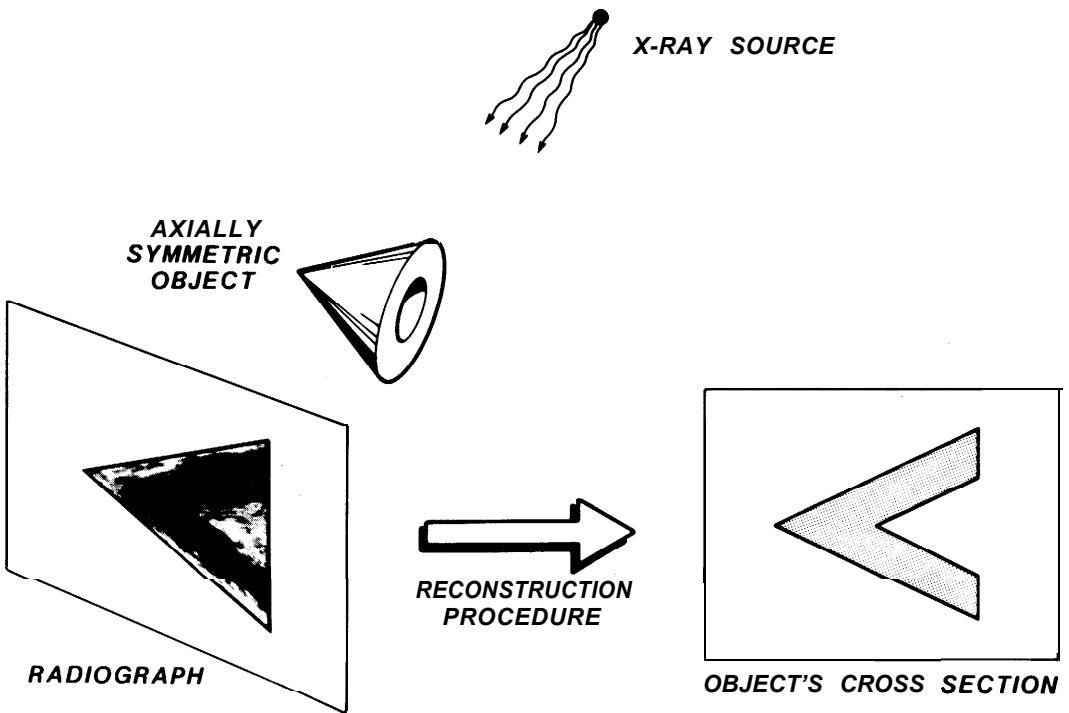


Figure 1: Overview of the tomographic method. An object with axial symmetry is radiographed with the radiographic axis perpendicular to the axis of symmetry. The reconstruction procedure transforms the radiograph into an estimate of the cross section of the object.

from the radiograph and the consequent increase in contrast with which it is possible to display the reconstruction.

Abel inversion has been considered over the years by many authors, most recently in [3,4,5,6]. It has even been scrutinized on a number of occasions by Milt Wing, together with various colleagues [7,8,9]. In its discrete form, Abel inversion is nonsingular except at the axis of symmetry. When projection measurements are derived from a radiograph of an object, they are nonlinearly related to the line integral of the linear attenuation values through the object. Near the center of a dense object, the optical density can approach the fog level of the film, resulting in a poor signal-to-noise ratio. This effect, together with the divergence of the Abel inversion at the axis, can result in overwhelming noise in that region of the reconstruction of the object's density. The growth of noise in the reconstruction can be controlled through a nonlinear maximum a *posteriori* (MAP) formulation in which the known uncertainty in the optical density data caused by film noise is balanced with the suspected smoothness in the object's density [10]. In this approach it is possible to include other constraints on the reconstruction, such as non-negativity. The usefulness of this approach is demonstrated by the reconstruction of a solid metal object with axial symmetry from a single radiograph. The MAP approach presented here may be of interest to applied mathematicians because it represents yet another means of obtaining a regularized solution in which prior knowledge about the object function can be incorporated in a consistent way.

2 Statement of the problem

The line integral along a line that is a distance R from the origin of a 2-D function possessing circular symmetry $f(r)$ is given by

$$p(R) = 2 \int_R^\infty \frac{f(r) r dr}{\sqrt{r^2 - R^2}}. \tag{1}$$

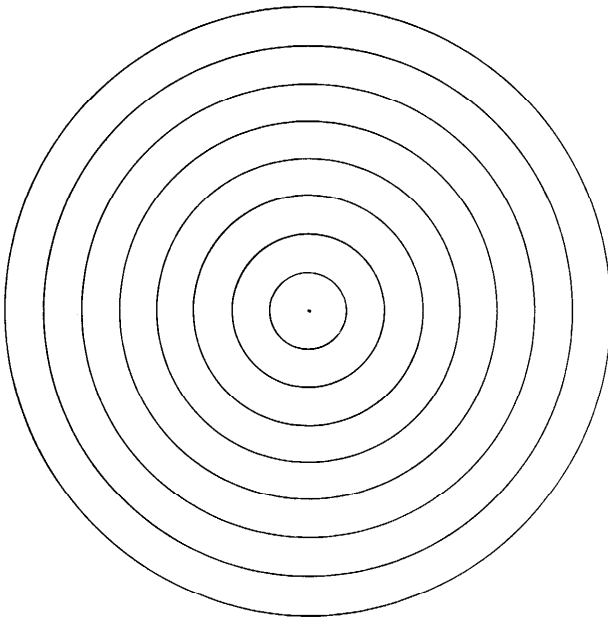
By a change of variables, Eq. (1) can be shown to be equivalent to the Abel transform. A solution for $f(r)$, given a known projection $p(R)$, was derived by Abel more than a century and a half ago [1]. Direct evaluation of the Abel inversion formula can lead to mathematical difficulties, which can be overcome by a suitable revision of the formula [5]. An alternative approach based on a discrete model avoids these difficulties. An object with axial symmetry is considered to be composed of a series of nested annuli, as depicted in Fig. 2, whose amplitudes are to be determined. The outermost annulus, whose projection is shown in Fig. 2, is the only annulus that contributes to the ends of the projection interval. Thus, it is possible to determine the amplitude of the outermost annulus from these projection values and consequently its contributions to each inner projection sample. The same analysis is applied to the next annulus and so on until the center is reached. Hence, the solution is easily realized by ‘peeling the onion’ from the outside to the inside.

A minor variation in this model of nested annuli is useful. Each annulus of the simple model is replaced by two annuli. The density profiles of these two annuli vary as $\frac{1}{2}[1 + \cos(\theta)]$ and $\frac{1}{2}[1 - \cos(\theta)]$, where θ is the angle between the radiographic axis and the vector between the center of the annulus and its rim. Thus the density of each annulus varies linearly with the transverse distance from the center from zero on one side to full density on the other side. The tapers of the two annuli vary in opposite directions so that, if they are given equal amplitudes, the sum of both densities is the same as that of the original annulus. The result of this decomposition is that the major contribution to the reconstruction on each side of the rotation axis comes predominately from the corresponding side of the projection. This model of annuli with tapered densities is better than one in which the annuli on each side are considered to be entirely distinct because it smoothly bridges both sides. Thus, even when the left and right sides of a projection might otherwise dictate considerably different values at the origin (producing a discontinuity there), this tapered model will tend to produce a smoothly varying reconstruction.

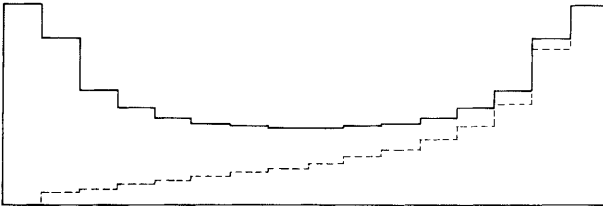
In this discrete model, the relationship between the discretely sampled projections, represented by the vector p , and the amplitudes of the corresponding annuli, represented by the vector f , is given by

$$p = Hf,$$

where H is the measurement matrix. The H matrix is explicitly displayed for a projection of 10 discrete samples in Fig. 3. For this model H possesses a bow-tie structure so that Eq. (2) is easy to solve by a procedure similar to Gaussian elimination in which the unknowns are determined alternatively from the top and bottom of the set of equations. If the tapered aspect of the model were not employed, H would have a lower triangular form and straightforward Gaussian elimination could be used.



MODEL OF AXISYMMETRIC OBJECT



PROJECTION OF OUTER ANNULUS

Figure 2: Model of a 2-D object with circular symmetry composed of a series of annuli whose widths correspond to the width of a pixel in the discretely sampled projection. Below is the projection of the outer annulus. The dashed line shows the projection of the outer annulus when its density is assumed to vary linearly from zero on the left side to full density on the right.

4.088	0.000	0.000	0.000	0.000	0.000	0.000	0.000	0.000	0.000
3.083	3.626	0.000	0.000	0.000	0.000	0.000	0.000	0.000	0.385
1.893	2.660	3.097	0.000	0.000	0.000	0.000	0.000	0.443	0.541
1.420	1.598	2.157	2.457	0.000	0.000	0.000	0.539	0.639	0.710
1.121	1.159	1.236	1.504	1.571	0.000	0.752	0.824	0.870	0.896
0.896	0.870	0.824	0.752	0.000	1.571	1.504	1.236	1.159	1.121
0.710	0.639	0.539	0.000	0.000	0.000	2.457	2.157	1.598	1.420
0.541	0.443	0.000	0.000	0.000	0.000	0.000	3.097	2.660	1.893
0.385	0.000	0.000	0.000	0.000	0.000	0.000	0.000	3.626	3.083
0.000	0.000	0.000	0.000	0.000	0.000	0.000	0.000	0.000	4.088

Figure 3: The \mathbf{H} matrix, which describes the projection measurements in the model shown in Fig. 2 for a projection consisting of 10 discrete samples.

The projections needed as input for tomographic reconstruction, Eq. (2), may be obtained from radiographic measurements. Suppose that a 3-D object is radiographed with an essentially monoenergetic x-ray source. If the x-rays are detected by a direct-recording film, the optical density of the developed film is proportional to the x-ray intensity. At the intersection of each line segment L that originates at the point source with the film plane, the optical density of the film is given by

$$D(p) = D_0 + D_1 \exp \{-p\}, \tag{3}$$

where the pathlength p is the line integral along line L of the object's linear attenuation coefficient distribution $\mu(x, y, z)$, evaluated at the x-ray energy. In the above equation, D_0 is the background density of the film, which includes the fog level of the film and any contribution from scattered radiation and D_1 is the net density (above D_0) that would be obtained in the absence of the object. Figure 4 illustrates this relationship. The highly nonlinear behavior of Eq. (3) for optical densities near D_0 makes the reconstruction there very sensitive to the choice for D_0 . This consideration points out the need to know D_0 very accurately to avoid making serious systematic errors in the reconstruction. Slight variations in D_0 arising from variations in the scattered radiation field may be difficult to take into account.

Putting Eqs. (2) and (3) together, we obtain the overall measurement equation for the measured optical density vector \mathbf{g}

$$\mathbf{g} = s\{\mathbf{Hf}\}, \tag{4}$$

where, in a change of notation to be consistent with that of Hunt [11], the attenuation law is now represented by the function $s\{\mathbf{p}\}$, which operates on each individual component of the pathlength vector $\mathbf{p} = \mathbf{Hf}$ with the nonlinear scalar function given by Eq. (3). Under certain circumstances, direct inversion of Eq. (4) is possible

$$\hat{\mathbf{f}} = \mathbf{H}^{-1} s^{-1}\{\mathbf{g}\}. \tag{5}$$

This inverse only exists, however, if \mathbf{H} is nonsingular (possesses no null space). Such is the case for the discrete model of the Abel transformation. However, difficulty can arise in inverting the nonlinear transformation s . When the measured density \mathbf{D} is either above $D_0 + D_1$ or below D_0 , which is possible because of noise fluctuations, Eq. (3) cannot be meaningfully inverted. The MAP method overcomes this difficulty.

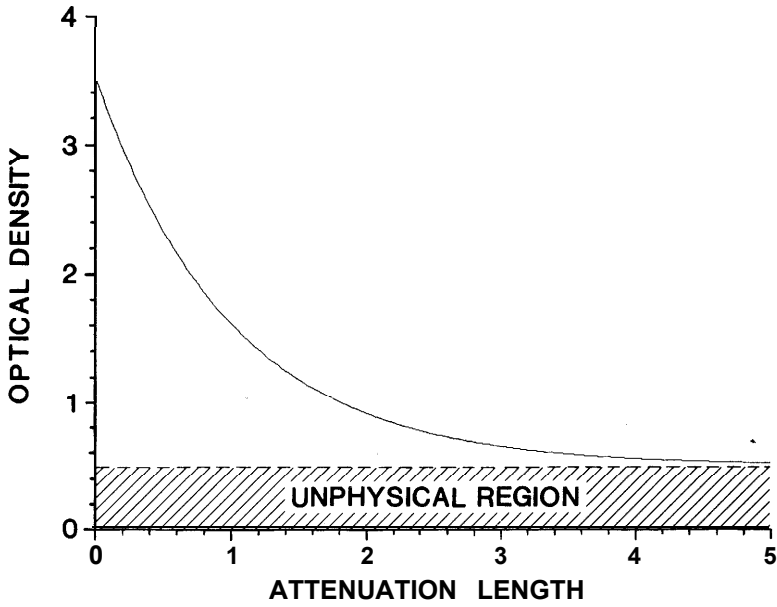


Figure 4: The measurement of x-ray attenuation by film is given by an exponential in the optical density. Values of the optical density below the fog level D_0 , 0.5 in this diagram, are theoretically not allowed.

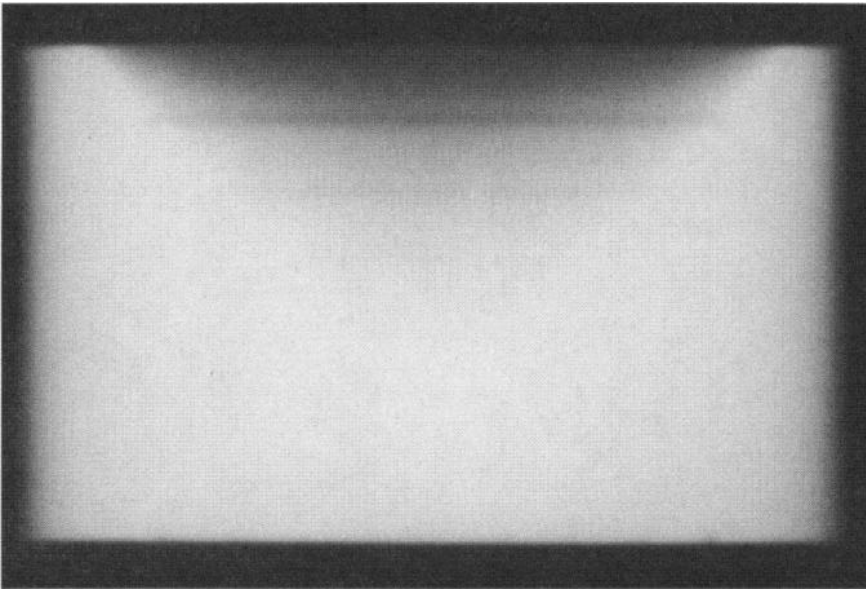


Figure 5: Radiograph of an axially symmetric steel object.

Now consider a 3-D object that possesses axial or rotational symmetry. In any plane that is perpendicular to the symmetry axis, the object's cross section has circular symmetry. If the object is radiographed with a set of parallel x-ray beams all of which lie in such a plane, the pathlengths obtained by applying Eq. (3) will correspond precisely to those in the 2-D situation. Thus, the radial distribution of that cross section can be reconstructed. A line-by-line analysis carried out in this way on each line of the radiograph that is perpendicular to the symmetry axis then yields the complete radial distribution of the object.

Figure 5 displays a radiograph of a test object with axial symmetry. The object is a 70-mm-long right circular steel cylinder, 120 mm in diameter, with a 45° cone removed from one end to a depth of 40 mm. Four 2-mm-square grooves were machined on the flat face as well as on the inside of the cone. The radiograph was taken with a Co-60 source using Kodak AA industrial radiographic film placed in close contact with 0.25-mm-thick lead screens, front and back. The object was placed with its axis of symmetry perpendicular to the radiographic axis in a geometry to closely approximate the parallel beam assumed by the reconstruction procedure. Figure 5 is actually a digital image, 220 by 150 pixels in size with pixel spacing of 0.6 mm. It is displayed here with a contrast comparable to that in the original radiograph. The grooves with the smallest diameters are virtually impossible to see because of their extremely low contrast on the radiograph. The diffuse densities in the radiograph range from about 0.5 to 3.5, the latter corresponding to that produced by the unattenuated x-ray beam.

When the tomographic reconstruction indicated by Eq. (5) is performed on each line of the radiograph, Fig. 5, and the reconstructed radial profiles are combined to form an image, Fig. 6 results. This reconstruction closely resembles the cross section of the object itself. The value of the linear attenuation coefficient reconstructed for the steel is approximately the same as the tabulated value for iron at 1.25 MeV, namely 0.042 mm^{-1} . The grooves, which were very difficult to observe in the original radiograph, are

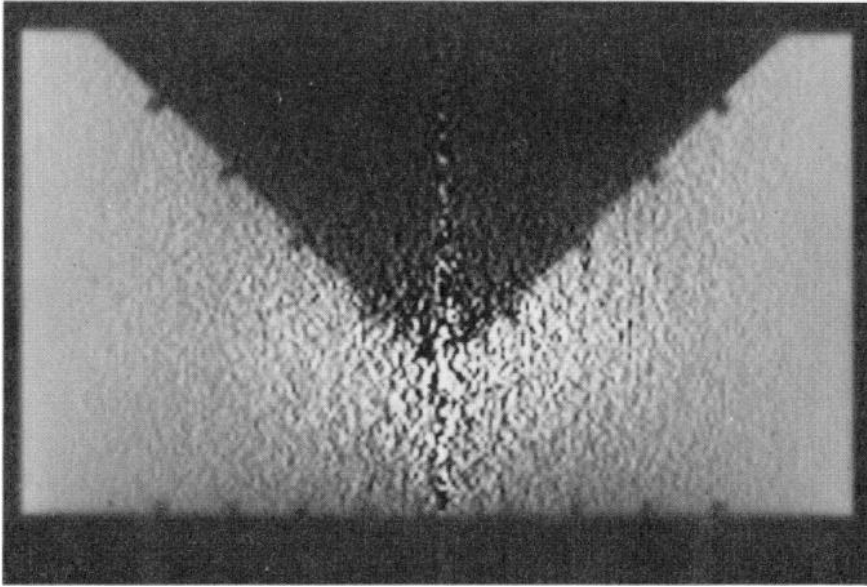


Figure 6: The reconstruction of the cross section of the object derived from Fig. 5. The 2-mm-square grooves machined in the inner cone and on the end face are much more readily visible. These grooves were nearly invisible in the original radiograph.

now easily seen. The tomographic reconstruction procedure has redisplayed the data in such a way that one's ability to derive information from the image is limited by the inherent noise, which was not the case for the original radiograph. The attainment of the ultimate limit in image interpretation dictated by the noise is one of the major goals of image processing!

However, there is severe enhancement of the noise near the axis of symmetry that arises from a nearly singular condition in the reconstruction procedure there. This near singularity is equivalent to the physical statement that as a ring of material with constant thickness decreases in diameter, it produces a smaller and smaller optical-density signal on the radiograph, making it increasingly 'difficult to observe in the presence of nearly constant film-density noise. The uncontrolled growth of noise in the reconstruction poses difficulty for visual interpretation of the image. The human eye simply cannot perform the necessary averaging over noise of such large amplitude. One possible method to control the noise in the reconstruction is to employ nonlinear maximum *a posteriori* probability (MAP) restoration [2], to be discussed next.

The Bayesian Approach

The essence of the Bayesian approach is the assumption that the image to be reconstructed is a random selection from an identifiable ensemble of similar images. In the context of medical imaging, an example of such an ensemble is the collection of all hearts imaged in the same kind of procedure. By using this prior information about the type of image that is expected, one anticipates that the null-space component of the reconstruction might be meaningfully estimated, thereby reducing artifacts. The Bayesian

approach provides a way to incorporate prior information about the structure of the reconstructed object into the solution. Of course, other types of prior information can also be incorporated in the Bayesian method of reconstruction. See Refs. [12,13] for a more complete description of the general situation.

Direct inversion of the measurement equations using Eq. (5) tacitly assumes the measurements can be made with infinite accuracy. In reality, all measurements of continuous quantities are subject to random fluctuations called noise. Thus, the measurements should be written as

$$\mathbf{g} = s\{\mathbf{Hf}\} + \mathbf{n} , \tag{6}$$

where \mathbf{n} is the noise vector. It must be emphasized that the noise vector is a random variable. It is different for each set of measurements, and its exact value cannot be correctly guessed. Each realization of the vector \mathbf{n} may be regarded as a random selection from an infinitely large ensemble, or collection, of noise vectors. In general, the noise fluctuations may possess an arbitrary probability density distribution. Frequently, the assumption is made that the noise has a multivariate Gaussian distribution with a zero mean

$$\mathbf{P}(\mathbf{n}) \sim \exp\left\{-\frac{1}{2}\mathbf{n}^T \mathbf{R}_n^{-1} \mathbf{n}\right\} , \tag{7}$$

where \mathbf{R}_n is the noise covariance matrix, of which the ij element is

$$[\mathbf{R}_n]_{ij} = \langle n_i n_j \rangle . \tag{8}$$

The assumption of a normal distribution is often valid. The brackets () indicate an average taken over all members of the ensemble of noise vectors. The above expression is general enough to fully characterize noise fluctuations that depend upon the strength of the signal being measured or upon the position of the measurement. It can even take into account correlations in the noise. By its definition, \mathbf{R}_n is a positive-definite matrix, and its inverse, needed in Eq. (7), is assured.

Under a wide range of reasonable conditions [14], when averaged over the full ensembles of noise and images, the best estimate for the reconstruction is that particular image \mathbf{f} which maximizes the a *posteriori* conditional probability density of \mathbf{f} given the measurements \mathbf{g} . This probability is given by Bayes' formula

$$P(\mathbf{f}|\mathbf{g}) = \frac{P(\mathbf{g}|\mathbf{f})P(\mathbf{f})}{P(\mathbf{g})} \tag{9}$$

in terms of the conditional probability of \mathbf{g} given \mathbf{f} , $P(\mathbf{g}|\mathbf{f})$, and the a *priori* probability distributions of \mathbf{f} and \mathbf{g} separately, $P(\mathbf{f})$ and $P(\mathbf{g})$.

Hunt [11] proposed using the Bayesian approach for improved image recovery. It is assumed that $P(\mathbf{g}|\mathbf{f})$ is given by $P(\mathbf{n})$, in which \mathbf{g} is Gaussian distributed about the mean $s\{\mathbf{Hf}\}$, as in Eq. (7),

$$P(\mathbf{g}|\mathbf{f}) \sim \exp\left\{-\frac{1}{2}(\mathbf{g} - s\{\mathbf{Hf}\})^T \mathbf{R}_n^{-1} (\mathbf{g} - s\{\mathbf{Hf}\})\right\} . \tag{10}$$

This conditional probability may be referred to as the probability density distribution of the measurements, since it follows solely from the distribution of the error fluctuations in

the measurements. It is also often called the likelihood function [14]. The *a priori* probability density function for the ensemble of images $P(\mathbf{f})$ is assumed to be a multivariate Gaussian distribution with a mean value $\bar{\mathbf{f}}$ and with a covariance matrix \mathbf{R}_f :

$$P(\mathbf{f}) \sim \exp \left\{ -\frac{1}{2} (\mathbf{f} - \bar{\mathbf{f}})^T \mathbf{R}_f^{-1} (\mathbf{f} - \bar{\mathbf{f}}) \right\}. \quad (11)$$

Under these assumptions, the maximum *a posteriori* (MAP) solution is easily shown to satisfy [11] the MAP equation

$$\mathbf{R}_f^{-1} (\bar{\mathbf{f}} - \mathbf{f}) + \mathbf{H}^T \mathbf{S}_b \mathbf{R}_n^{-1} (\mathbf{g} - s\{\mathbf{H}\mathbf{f}\}) = \mathbf{0}, \quad (12)$$

where \mathbf{S}_b comes from the derivative of s :

$$\mathbf{S}_b = \text{diag} \left(\left. \frac{\partial s(u)}{\partial u_i} \right|_{u_i = b_i} \right) \quad (13)$$

evaluated at the arguments of s

$$b_i = \{\mathbf{H}\mathbf{f}\}_i. \quad (14)$$

The transpose of \mathbf{H} is the familiar backprojection operation in the context of tomographic reconstruction. The first term comes from the derivative of $\mathbf{P}(\mathbf{f})$, given by Eq. (11), and the second from $P(\mathbf{g}|\mathbf{f})$, Eq. (10). It can be seen that the MAP solution strikes a balance between its deviation from the ensemble mean $\bar{\mathbf{f}}$ and the solution to the measurement equation, Eq. (4). This balance is controlled by the covariance matrices \mathbf{R}_f and \mathbf{R}_n that specify the confidence with which each deviation is weighted, as well as possible correlations between the deviations.

If s were a linear function, Eq. (12) would be linear in the unknown vector \mathbf{f} . This linearity follows from the assumption of normal distributions for the *a priori* and measurement-error probability densities. In this circumstance, the MAP reconstruction method is equivalent to the minimum-variance linear estimator with nonstationary mean and covariance ensemble characterizations [14]. It is also called the minimum mean-square-error method [15]. When the blur function, noise, and ensemble image properties are stationary (do not depend upon position), then \mathbf{H} , \mathbf{R}_f , and \mathbf{R}_n are Toeplitz matrices, and, in the circulant approximation, Eq. (12) is the same as the well-known Wiener filter [15]. The application of the linear MAP method to tomographic reconstruction was suggested by Herman and Lent [16].

We wish to address situations in which there is a lack of specific information about the object to be reconstructed. It is known that in such cases the use of the MAP method probably cannot provide much benefit in correcting for the null-space deficit in the reconstruction [12,13]. In the present case of Abel inversion, this deficit exists only for the nonlinear transformation s , not for the matrix \mathbf{H} . Suppose that we wish to have a smooth solution unless the data legitimately indicate otherwise. Then a common choice for \mathbf{R}_f is

$$\mathbf{R}_f = (\nabla^2 \nabla^2)^{-1}. \quad (15)$$

Since $\nabla^2 \nabla^2$ is a differentiation operator, \mathbf{R}_f is a smoothing operator. Since, in the absence of very accurate data, we would like the solution to approach something smooth, we further choose for $\bar{\mathbf{f}}$ a smooth version of the estimate \mathbf{f}

$$\bar{\mathbf{f}} = \mathbf{R}_f \mathbf{f}. \quad (16)$$

In our calculations \mathbf{R}_f is calculated by using a filter that behaves as the inverse fourth power of the spatial frequency. The addition of a small regularizing term avoids blowup at zero frequency. The amount of regularization controls the width of the smoothing function, which in our example is chosen to have a full-width at half-maximum of 11 pixels. To avoid making the analysis any more complicated than necessary, we will assume that the noise in the radiographic measurements is stationary and uncorrelated. Then,

$$\mathbf{R}_n = \sigma_n^2 \mathbf{I}, \tag{17}$$

where σ_n^2 is the variance of the noise. While this assumption may not be completely valid, it is a sufficiently good approximation in most instances. Since it is desirable to control its strength, \mathbf{R}_f is multiplied by the factor λ , whose value is adjusted to make the rms residuals approximately match the value expected for the noise. The net effect on the MAP equation, Eq. (12), is that \mathbf{R}_n disappears and the coefficient of the \mathbf{H}^T term becomes λ/σ_n^2 .

There is a close relationship between the method just described and that of constrained least squares (CLS) [15]. In the latter method, the solution minimizes the norm of some linear operator applied to \mathbf{f} , subject to the constraint that the rms residuals match a specified value. In fact the above choice for \mathbf{R}_f amounts to seeking the solution with minimum curvature. However, the usual version of CLS does not make reference to $\bar{\mathbf{f}}$ and, in effect, assumes $\bar{\mathbf{f}} = 0$. Clearly this is not a very good choice for $\bar{\mathbf{f}}$, as it is the default value when the data are very noisy. In noisy regions our choice pushes the solution towards a smoothed value instead of zero, as does the usual CLS algorithm.

Andrews and Hunt [15] suggested that the maximum-entropy algorithm may be viewed as an alternate form of the constrained least-squares approach. This connection is most easily seen from the work of Gull and Daniell [17], in which they merge the maximum-entropy principle with the probabilistic concepts of random noise. They propose that one find the solution that maximizes entropy, subject to the constraint that the calculated rms residuals be equal to a predetermined value. The similarity between the function they wish to minimize and the quadratic form that leads to the MAP equation, (12), prompts one to interpret the maximum-entropy technique in terms of a Bayesian approach [] in which the a priori probability density has a particular form [13]. Independent of whether this Bayesian interpretation is correct or not, the performance of the maximum-entropy algorithm can be understood and interpreted in terms of what one would expect for MAP for that particular prior probability distribution.

4 An Iterative Solution Technique

We have adopted an iterative approach to the solution of Eq. (12) based on the scheme proposed by Hunt [11]. The iteration scheme is given by:

$$\mathbf{f}^0 = \bar{\mathbf{f}} \tag{18}$$

$$\mathbf{f}^{k+1} = \mathbf{f}^k + c^k \mathbf{r}^k \tag{19}$$

$$\mathbf{r}^k = \mathbf{R}_f^{-1}(\bar{\mathbf{f}} - \mathbf{f}^k) + \mathbf{H}^T \mathbf{S}_b \mathbf{R}_n^{-1}(\mathbf{g} - s\{\mathbf{H}\mathbf{f}^k\}) \tag{20}$$

$$c^k = \frac{\mathbf{r}^{kT} \mathbf{q}^k}{\mathbf{q}^{kT} \mathbf{q}^k} \quad (21)$$

$$\mathbf{q}^k = (\mathbf{R}_f + \mathbf{H}^T \mathbf{S}_b \mathbf{R}_n^{-1} \mathbf{S}_b \mathbf{H}) \mathbf{r}^k \quad (22)$$

where vector \mathbf{r}^k is the residual of Eq. (12), and the scalar c^k is chosen by Eq. (21) to minimize the norm of \mathbf{r}^k . When the residual goes to zero, the corresponding \mathbf{f}^k is clearly a solution of the MAP Eq. (12). This iterative scheme is very similar to the one proposed by Herman and Lent [16] for linear MAP image restoration. Their update scheme consisted in incrementing \mathbf{f}^k by Eq. (20) multiplied by \mathbf{R}_f , avoiding a potential computational difficulty if \mathbf{R}_f is nontrivial. But it has the disadvantage of providing smooth update vectors. Consequently, it becomes very difficult to achieve good high-frequency response.

We have found that the above scheme does not work well for this problem even though it was adequate for the usual 2-D reconstruction case [12]. To obtain better convergence, we have added a few variations. Instead of using only one update vector, as in Eq. (19), we have used a second vector, alternatively switching between \mathbf{q}^k and the vector

$$\mathbf{H}^{-1}(\mathbf{g} - s\{\mathbf{H}\mathbf{f}^k\}), \quad (23)$$

which is similar to the inverse, Eq. 5. We note that the use of the inverse directly did not appear to work as it overcorrected the residuals. The coefficients for each of the updating vectors are computed in a manner similar to that given by Eq. (21). This iteration scheme encompasses the modification to Hunt's procedure that was suggested by Trussell and Hunt [19], but with a different choice for the normalization of the update vectors. A scheme similar to that of conjugate gradient was also tried in which each update is constructed to be orthogonal to preceding ones. It appeared to be of little use in improving convergence. We did find it helpful to gradually admit successively higher frequency components to the solution, which is accomplished by low-pass filtering of the update vectors and progressively increasing the cutoff frequency of the filter as the number of iterations increases. For the low-pass filter we used a Gaussian function centered on zero frequency. In our example we used 10 iterations. The half-value frequency of the low-pass filter ranged from 0.210 to 1.0 times the Nyquist frequency, stepping by a factor of 1.189 after each iteration. The computation time on a VAX 8700 was 45 minutes for the MAP reconstruction of 150 lines, each 220 pixels long, compared with one minute for direct inversion.

An advantage to any iterative reconstruction scheme is that constraints may be readily placed upon the reconstructed function \mathbf{f}^{k+1} after each update. Such constraints include upper and lower limits to the reconstruction value, known region of support, etc.

The application of the above MAP technique to the earlier reconstruction problem yields Fig. 7, which shows that the extreme noise fluctuations in Fig. 6 have been controlled well. However, the sharp response to the outer edge of the cylinder is preserved. By reducing extremely large noise fluctuations, the result is rendered more acceptable to the eye [20]. This wide light region near the vertex of the cone probably arises from a slight shift in D_0 caused by variation in the scattered radiation background. Figure 8 shows a comparison between the MAP and direct inversion techniques for a single line taken from the radiograph.

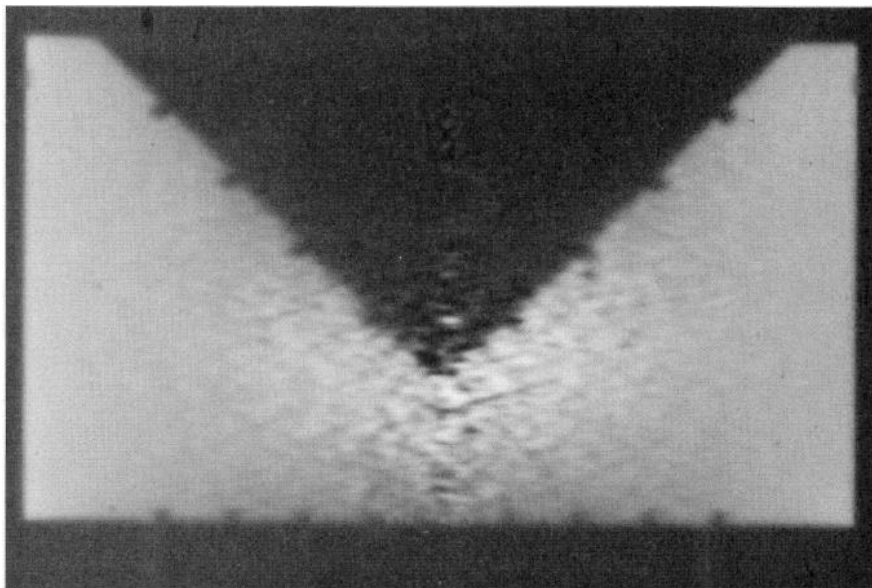


Figure 7: The MAP reconstruction derived from Fig. 5 using $\lambda = 2.0 \times 10^{-5}$ and $\sigma_{\text{nl}} = 0.01$. Note that in the noisy regions the amplitude of the noise has been reduced relative to that in Fig. 6, while at the same time maintaining excellent resolution at the outer edge.

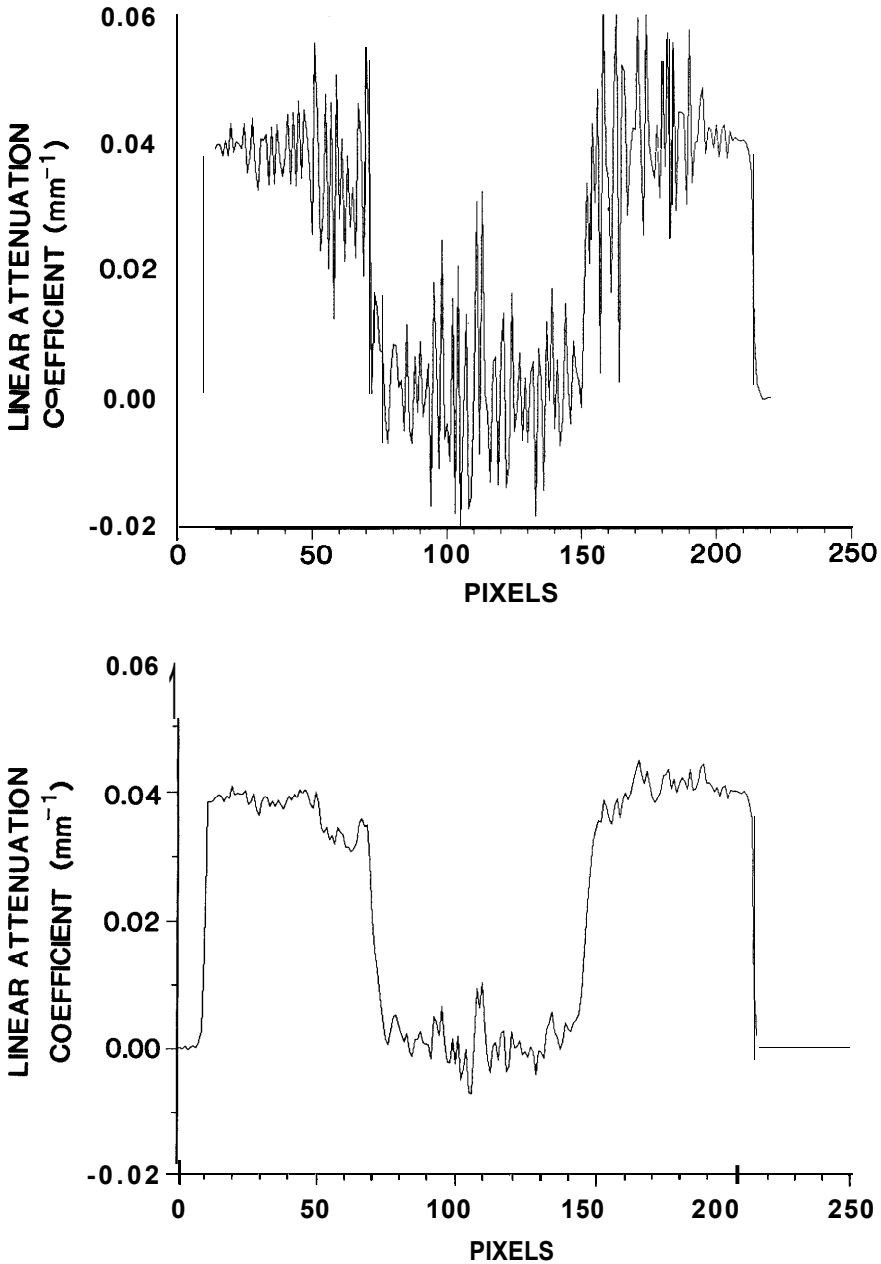


Figure 8: A comparison for one line of data between the reconstruction (top) obtained by direct inversion of the measurement equations and that (bottom) obtained by the MAP technique.

5 Conclusions

It has been shown that the extension of Abel inversion to the reconstruction of a 3-D axially symmetric object from a single radiograph offers significant benefits as an image analysis tool. It has been demonstrated that the noise amplification caused by the nearly singular Abel inversion and the potential difficulty in the inversion of the nonlinear radiographic measurements can be controlled using the MAP method with a simplified choice of a smoothed value of f for \bar{f} and a smoothing operator for \mathbf{R}_f . With these choices the MAP algorithm is similar to the constrained least-squares method [15] corresponding to minimum curvature. We have employed a multifaceted iterative reconstruction algorithm to find the solution with the maximum a *posteriori* probability.

In general the Bayesian approach permits the incorporation of information about the general shape or structure of the object to be reconstructed. Supposing a lack of prior knowledge about the object to be reconstructed, we have only assumed that the reconstructed function should be smooth unless otherwise dictated by the data. If more prior information is available, it may be desirable to incorporate it into the solution. However, one must be careful not to 'load the dice' too heavily or one will obtain only the expected result [13].

Acknowledgments

I wish to express my appreciation to George Brooks for providing the excellent radiographs used in the static example. I have benefited from many fruitful discussions with Rollin Whitman and Allen Mathews.

References

- [1] N. H. Abel. Résolution d'un problème de mécanique. *J. Reine u. Angew. Math.*, 1:153-157, 1826.
- [2] K. M. Hanson. Tomographic reconstruction of axially symmetric objects from a single radiograph. In *Proc. 16th Inter. Cong. on High Speed Photography and Photonics. (Proc. SPIE, 491:180-187)*, Strasbourg, 1984.
- [3] R. W. Porter. Numerical solution for local emission coefficients in axisymmetric self-absorbed sources. *SIAM Rev.*, 6:228-242, 1964.
- [4] S. Corti. The problem of Abel inversion in the determination of plasma density from phase measurements. *Let. Nuovo Cim.*, 29:25-32, 1980.
- [5] M. Deutsch and I. Beniaminy. Derivative-free inversion of Abel's integral equation. *Appl. Phys. Lett.*, 41:27-28, 1982.
- [6] M. Deutsch. Abel inversion with a simple analytic representation for experimental data. *Appl. Phys. Lett.*, 1983.

- [7] D. S. Carter, G. Pimbley, and G. M. Wing. *On the unique solution for the density function at PHERMEX*. Technical Report T-5-2023, Los Alamos Scientific Laboratory, 1957.
- [8] R. MacRae and G. M. Wing. Some *remarks on problems connected with data analysis in PHERMEX*. Technical Report T-5-2043, Los Alamos Scientific Laboratory, 1958.
- [9] V. Faber and G. M. Wing. *The Abel integral equation*. Technical Report LA-11016-MS, Los Alamos National Laboratory, 1987.
- [10] K. M. Hanson. A Bayesian approach to nonlinear inversion: Abel inversion from x-ray attenuation data. Presented at the Fourth Workshop on Maximum Entropy and Bayesian Methods (unpublished), Calgary, August 6-8, 1984.
- [11] B. R. Hunt. Bayesian methods in nonlinear digital image restoration. *IEEE Trans. Comp.*, C-26:219-229, 1977.
- [12] K. M. Hanson and G. W. Wecksung. Bayesian approach to limited-angle reconstruction in computed tomography. *J. Opt. Soc. Amer.*, 73:1501-1509, 1983.
- [13] K. M. Hanson. Bayesian and related methods in image reconstruction from incomplete data. In *Image Recovery: Theory and Application*, Henry Stark, ed., Academic, Orlando, 1987.
- [14] A. P. Sage and J. L. Melsa. *Estimation Theory with Applications to Communications and Control*. Robert E. Krieger, Huntington, 1979.
- [15] H. C. Andrews and B. R. Hunt. *Digital Image Restoration*. Prentice-Hall, Englewood Cliffs, New Jersey, 1977.
- [16] G. T. Herman and A. Lent. A computer implementation of a Bayesian analysis of image reconstruction. *Inform. Contr.*, 31:364-384, 1976.
- [17] S. F. Gull and G. J. Daniell. Image reconstruction from incomplete and noisy data. *Nature*, 272:686-690, 1978.
- [18] H. J. Trussell. The relationship between image reconstruction by the maximum a posteriori method and a maximum entropy method. *IEEE Trans. Acoust., Speech, Signal Processing*, ASSP-28:114-117, 1980.
- [19] H. J. Trussell and B. R. Hunt. Improved methods of maximum a posteriori restoration. *IEEE Trans. Comput.*, C-27:57-62, 1979.
- [20] K. M. Hanson. Image processing: mathematics, engineering, or art? In *Proc. Application of Photo-Optical Instrumentation in Medicine XIII. (Proc. SPIE, 535:70-81)*, Newport Beach, 1985.